metals

MDPI

Article

The Triaxiality Effect on Damage Evolution in Al-2024 Tensile Samples

Álvaro González [1], Diego Celentano [2], Marcela Cruchaga [3] and Jean-Philippe Ponthot [4,*]

[1] Escuela de Ingeniería Mecánica, Pontificia Universidad Católica de Valparaíso, Quilpué 2430000, Chile; alvaro.gonzalez.o@pucv.cl
[2] Departamento de Ingeniería Mecánica y Metalúrgica, Pontificia Universidad Católica de Chile, Macul 7810000, Chile; dcelentano@uc.cl
[3] Departamento de Ingeniería Mecánica, Universidad de Santiago, Estación Central 9160000, Chile; marcela.cruchaga@usach.cl
[4] Department of Aerospace and Mechanical Engineering, Université de Liège, 4000 Liège, Belgium
* Correspondence: jp.ponthot@uliege.be

Abstract: The effect of triaxiality on the evolution of damage in Al-2024 aluminum cylindrical specimens is studied in this work. Uncoupled and coupled damage models, all of them explicitly dependent on triaxiality, are assessed and compared. These models are characterized by tensile tests on cylindrical specimens without notches, to obtain the material parameters for each model. The capability of each model to predict fracture when different positive triaxial conditions evolve is then evaluated through tensile tests on notched cylindrical specimens. In particular, the damage index, evaluated at the fracture strain level, is compared with the experimental results validating the models. Moreover, the triaxiality evolution in the different specimens is studied in order to assess its effect on damage, demonstrating that the fracture strain decreases at greater triaxiality values. Observations through scanning electron microscopy confirm this pattern; i.e., an increase in triaxiality reveals a shift in the fracture mechanism from a more ductile condition in the original specimens to a more brittle one as the notch radius decreases. In addition, bilinear damage evolution is proposed to describe the physical behavior of the material when the Lemaitre coupled model is considered. In such a case, special attention must be devoted to the material characterization since coupling between hardening material parameters and damage affects the results.

Keywords: damage; fracture; triaxiality; notched tensile samples; model comparison; validation

Citation: González, A.; Celentano, D.; Cruchaga, M.; Ponthot, J.-P. The Triaxiality Effect on Damage Evolution in Al-2024 Tensile Samples. *Metals* **2024**, *14*, 1103. https://doi.org/10.3390/met14101103

Academic Editor: Alberto Campagnolo

Received: 30 July 2024
Revised: 22 September 2024
Accepted: 24 September 2024
Published: 26 September 2024

1. Introduction

Ductile fracture is characterized, from a macroscopic point of view, by presenting high levels of plastic deformation and a low speed of crack propagation. Furthermore, higher strain energy levels are required than in the case of brittle fracture. When studying ductile fracture from a microscopic point of view, it has been observed that this is the result of the nucleation, growth, and subsequent coalescence of micro-cavities induced by the high levels of deformation in the material [1–3].

Triaxiality has been shown to play an important role in fracture development [4] due to the fact that the stress state has a substantial effect on the ductile fracture mechanism, particularly on void growth and coalescence [5,6]. High levels of triaxiality have been achieved by tensile tests on notched specimens, both in flat [7–11] and cylindrical [12–15] specimens, showing that ductility and the plastic strain at the fracture stage decreased with increasing stress triaxiality [16–18]. Not only high levels of triaxiality have been studied [7–15], but also low [19–21] and negative [22–24] ranges of triaxiality. A micromechanical approach has also been considered in some works, with the intention of relating the incidence of triaxiality in the growth and coalescence of microcavities [25–28].

The effect of triaxiality on fracture has also been studied in aluminum alloys, with both experimental and computational approaches [29–35]. Bao and Wierzbicki [36] carried out an extensive experimental campaign including upsetting tests, shear tests, and tensile tests on 2024-T351 aluminum alloy, providing clues to fracture ductility for a wide range of stress triaxiality, showing that for negative stress triaxiality, the fracture is governed by shear mode; for large triaxialities, void growth is the dominant failure mode; and at low levels of stress triaxialities between these two regimens, the fracture may develop as a combination of shear and void growth modes. Ganjiani [5] used the experimental tests on aluminum alloy 2024-T351 specimens carried out by Bao and Wierzbicki [36] to validate his damage model that predicts fracture at both high and low levels of triaxiality, demonstrating that in this alloy, the fracture strain decreases when triaxiality increases. Kou et al. [37] studied the effect of stress triaxiality on mechanical properties of 6061 aluminum alloy extruded profiles with different specimens, and their results showed that the dimple morphology of the fracture section changes depending on the triaxiality values achieved.

To date, different models have been proposed that attempt to predict the conditions under which the material will be in a critical zone, where fracture could begin. Each of the different models proposed has advantages and disadvantages when it comes to predicting material failure, depending on the process in which it is evaluated and the material used [38–42]. Among the models available in the literature, a classification has been made between uncoupled and coupled damage models [43–45]. Those that incorporate a parameter that quantifies the degradation of the material subjected to stress in their constitutive equations are considered as coupled models [2,3,46–48], while those that neglect the effects of damage on the yield surface and other material parameters (e.g., Young's modulus and Poisson's ratio) are considered as uncoupled models [1,4,49–53].

Damage models based on stress triaxiality are widely used in predicting the ductile fracture process, including uncoupled and coupled approaches. To the best of our knowledge, the sensitivity of some coupled damage models (such as those described in [2,46,54,55]) to the variability of the stress triaxiality during the deformation history was only evaluated by La Rosa et al. [56]. Uncoupled models were not considered in such a work. Although this progress in the development and application of different damage models and materials over wide ranges of triaxialities is encouraging, further work is still needed, particularly regarding the effect of coupling damage to the evolution of internal variables that in turn affect triaxiality.

The present work reports on physical experiments and numerical simulations of tensile tests in smoothed and notched specimens to quantify the effect of positive triaxiality and compare the damage predicted by different uncoupled and coupled models, all of them explicitly dependent on triaxiality. The study encompasses experimental and numerical analyses. The material characterization based on the experimental data obtained from smoothed round specimens is first made based on the modified Voce hardening law. After that, the damage characterization is performed. For uncoupled models, the critical damage is obtained from numerical simulations. In the coupled damage model, the damage path is taken from the literature [57] and fitted with a recently proposed bilinear extension of Lemaitre's model [58]. Due to the coupled approach of this model, the damage affects the hardening law; therefore, the hardening parameters need to be readjusted with respect to parameters used in uncoupled situations. After that, tensile tests in notched specimens are simulated using the damage models previously characterized. The damage index, evaluated at the fracture strain level, is compared with the experimental results, validating the models. Moreover, triaxiality evolution in the different specimens is studied to assess the triaxiality effect on damage, focusing on the differences obtained after using uncoupled and coupled damage models. The main original aspects of the work are as follows: the experiments on smoothed and notched specimens are reported for a 2024 aluminum alloy, the numerical quantification of damage for both uncoupled and coupled approaches are presented and validated with the experimental data, a bilinear damage model is applied to different triaxiality conditions, and the differences in the evolution of the main

internal variables that affect triaxiality using uncoupled and coupled models is presented and discussed.

The paper is organized as follows. Materials, sample geometries, experimental procedures, damage models, hardening models, and numerical methods are presented in Section 2. Experimental results, uncoupled and coupled damage analyses, and triaxiality evolution are reported in Section 3 and discussed in Section 4. Finally, the conclusions are drawn.

2. Materials and Methods

This section encompasses the material and sample description, the experimental procedure, the damage and hardening models used in the study, and a brief description of the finite element method (FEM) applied in the simulations. The main objective is to provide a complete description of the methodology, both experimental and numerical, that will be used for the analysis of the results in the following sections. This section is divided into four parts. First, the experimental tests carried out in this work are presented. In the second and third parts, the analysis is carried out using uncoupled and coupled models, respectively. Finally, the results of the triaxiality evolution obtained with the different models in the different specimens are presented.

2.1. Material and Sample Geometries

The specimens used in this work were machined from cylindrical bars of an Al-2024 aluminum alloy. Two types of specimens were tested: a cylindrical specimen without notches with a nominal diameter of 6 mm, which considered a slight linear diameter reduction ($\phi = 5.94$) in the center to localize deformation (according to the ASTM-E8 standard [59]), and two cylindrical specimens with the same resistive diameter $\phi = 5.94$ mm but with two different levels of notch characterized by notch radii of R8 mm and R2.8 mm. The notched geometries were selected to provide a contrast with the triaxiality value of the unnotched case (which corresponds to a low triaxiality value). This approach aims to obtain not just one but two distinct geometries that can reach high triaxiality values. The details of the geometries of the specimens used in this study are presented in Figure 1.

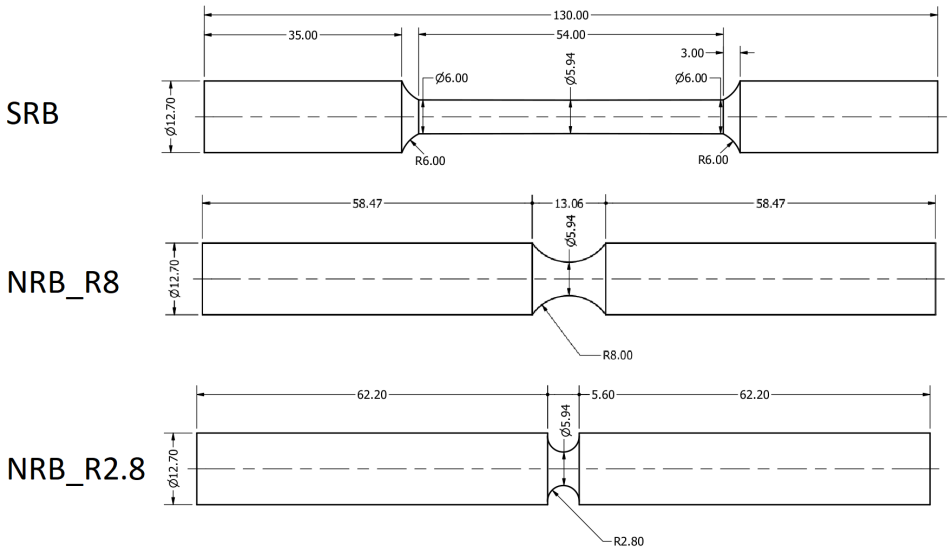

Figure 1. Uniaxial tensile cylindrical specimens with the same resistive diameter $\phi = 5.94$ mm: smoothed round bar (SRB) and notched round bars (NRB) with two different notch radii of 8 mm and 2.8 mm. (All dimensions are in millimeters.)

2.2. Experimental Procedure

Tensile tests were performed on a 10-ton Instron universal testing machine (Instron, Norwood, MA, USA) at a jaw speed of 5 mm/min. Each of the tests was conducted and

subsequently repeated three times to ensure the reliability and consistency of the results, with all measurements being carefully recorded and analyzed for accuracy. The force was registered using a load cell. The tests were recorded with a high-speed AOS Q series camera (AOS Technologies AG, Baden, Switzerland), which allowed for analysis using digital image correlation (DIC) to obtain the displacement and strain fields during the tests. DIC analysis was performed using the open-source software NCORR v1.2 [60]. The lens used was a 50 mm focal length lens, positioned at a working distance of approximately 400 mm from the specimen surface. A random speckle pattern was applied using spray paint to ensure high contrast, with a speckle size of approximately 0.03977 mm/pixel. The region of interest covered a length of 24 mm, focusing on the critical deformation zones. A digital extensometer was built and implemented through a Python subroutine that reads the strain data obtained via DIC. Both signals (force and strain) were synchronized, allowing for the construction of the corresponding stress–strain curves for each type of specimen tested. The experimental setup for the tests is presented in Figure 2.

Figure 2. Experimental setup of the tensile tests: an overview of 10-ton Instron universal testing machine, the force register system, and the high-speed camera used for employing digital image correlation.

The fractured specimens were subsequently analyzed using scanning electron microscopy (SEM) with the device shown in Figure 3. This technique allows a detailed examination of the fracture surface morphology with the intention of correlating the effect of triaxiality on changes in the fracture mechanism from a ductile to a more brittle response.

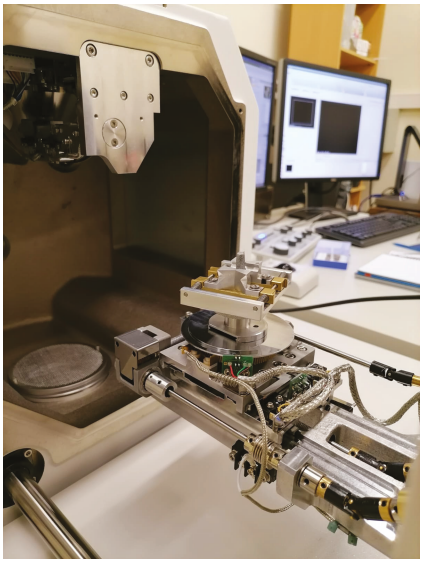

Figure 3. Specimen setup for SEM analysis.

2.3. Damage Models

Ductile fracture can be modeled under two different approaches: uncoupled and coupled damage models. A brief description of the models used in this work is given below.

2.3.1. Uncoupled Damage Models

Rice and Tracey [4] proposed a variational principle for the growth of cavities in a rigid plastic material that contains an internally spherical micro-void that is subjected to a remote stress field. The proposed principle is applied to different stress states to obtain a relationship that determines the behavior and evolution of the micro-void. Finally, the authors propose a criterion that considers the influence of triaxiality on the evolution of microcavities. The critical void radius is obtained when the fracture deformation is reached, which, when exceeded, supposes the initiation of the fracture process in the material.

Chaouadi [51] proposes a model where the damage of the material is studied from the expression given for the plastic work per unit volume. In this approach, it is assumed that in the plasticity stage, damage develops in the material through the growth of cavities. When the damage of the material exceeds a critical value (equivalent to when the effective plastic deformation exceeds the critical deformation), the fracture of the material begins. The Chaouadi model was used by McAllen and Phelan [47], who incorporated a modification based on what was proposed by Huang [61], where the growth of voids was evaluated for different levels of triaxiality.

The phenomenological approach of ductile fracture can be considered as a process of the accumulation of damage. In these criteria, the critical value can be determined by a combination of known stress–strain quantities. The Ayada model [52] considers the triaxiality effect on the plastic deformation path. The model proposed by Gonzalez et al. [53] weighs the effects of effective plastic strain and triaxiality in the evolution of the damage.

The damage index I_i for the models analyzed in this work are expressed in terms of the uncoupled damage functions f_i of each model i (listed in Table 1) as

$$I_i = \frac{1}{C_i} \int_0^{\bar{e}_p} f_i \cdot d\bar{e}_p \tag{1}$$

where $\bar{e}_p$ is the effective plastic strain. The damage index denotes the relationship between the damage achieved by each model, and the critical damage of each model C_i (material-dependent parameter). In this way, the damage index reaches the unit value when the calculated damage equals the critical damage, which is assumed as a fracture condition.

Table 1. Uncoupled damage functions explicitly depending on the triaxiality ξ analyzed in this work.

Rice and Tracey model	$f_1 = 0.283 \exp(1.5\xi)$	(2)
Modified Chaouadi model	$f_2 = \bar{\sigma}[1 + 1.461\xi^{\gamma} \exp(1.5\xi)]$ $\gamma = \begin{cases} 1.25 & for \quad 0 < \xi < 1 \\ 1.00 & for \quad \xi \geq 1 \end{cases}$	(3)
Ayada et al. model	$f_3 = \xi$	(4)
González et al. model	$f_4 = \xi^{\alpha} \bar{e}_p{}^{\beta}$	(5)

The relations presented in Table 1 (Equations (2)–(5)) are written in terms of the stress triaxiality ξ, where $\xi = \sigma_m/\bar{\sigma}$, such that σ_m is the mean stress and $\bar{\sigma}$ is the equivalent von Mises stress. All of these uncoupled models take into account the damage evolution only under positive triaxiality conditions. The parameters α and β are model parameters defined as in [53]. To obtain a global criterion to evaluate the damage when using different models during the analyses, and to avoid the use of uncertain local criteria, e.g., when only considering the maximum nodal value of the damage, an average damage value index $\overline{I}$ defined as

$$\overline{I} = \frac{\int_0^R (2\pi r I)dr}{\int_0^R (2\pi r)dr} \tag{6}$$

is adopted where r is the radial coordinate and R is the current specimen radius. According to Equation (6), the radial distribution of the damage index (I) at the central section of the specimen is weighted with the instantaneous area of such a section.

It is commonly observed in ductile materials that in cylindrical specimens subjected to uniaxial tension, fractures may initiate at the center of the specimen and propagate outward. However, this behavior can vary depending on the fracture mechanism and material microstructure. In this study, the previously defined criterion expressed by Equation (6) allows for the evaluation of the instant at which the specimen has reached total fracture and separated into two parts. To achieve a better understanding of the damage distribution, the damage values reached both at the center of the specimen and at the surface will be presented later, as well as the weighted average value according to this criterion.

2.3.2. Lemaitre Coupled Damage Model

The continuum damage mechanics (CDM) theory introduces an internal variable to quantify the material degradation, identified as damage d. Based on the original work proposed by Lemaitre [1], the formulation is written by Celentano and Chaboche [48] in term of the evolution equation for such internal variable ($\dot{d}$) as follows:

$$\dot{d} = A_d \frac{Y}{Y_{1D}} \dot{\bar{e}}_p \tag{7}$$

where A_d is the coupled damage function, $\dot{\bar{e}}_p$ is the evolution of effective plastic strain and Y is the damage–strain energy release rate (with Y_{1D} being this variable under uniaxial stress conditions) defined as

$$Y = \frac{\overline{\sigma}^2}{2\,E_0\,(1-d)^2}\,R_\nu \tag{8}$$

where E_0 is the Young's modulus of the undamaged material and R_ν is the stress triaxiality factor defined as

$$R_\nu = \frac{2}{3}(1+\nu) + 3(1-2\nu)(\xi)^2 \tag{9}$$

where ν is the Poisson's ratio.

The coupled damage function A_d describes the slope of the $d - \bar{e}_p$ curve for a uniaxial stress state. According to experiments carried out by Lemaitre, a linear relationship between damage and the plastic strain was found. Subsequently, experimental evidence has shown that this relationship is not always linear, and depending on the material that is studied, it can follow different paths [46]. A bilinear damage function (see Equation (10)) has recently been proposed [58] by adding a middle point that marks the change in the damage evolution slope, as can be seen in Figure 4. This model allows for three possible variations in void nucleation and growth behavior. In some materials, a large number of small voids nucleate once the threshold is reached, with new voids forming continuously until coalescence begins. In others, nucleation occurs at a moderate rate while existing voids grow as strain increases. Finally, in certain cases, only a few voids nucleate initially, but coalescence occurs when the strain approaches a critical value.

$$\dot{d} = \begin{cases} 0 & ;if\ \bar{e}_p < \bar{e}_0 \\ \dfrac{d_i}{\bar{e}_i - \bar{e}_0}\,\dot{\bar{e}}_p & ;if\ \bar{e}_0 < \bar{e}_p \leq \bar{e}_i \\ \dfrac{d_c - d_i}{\bar{e}_c - \bar{e}_i}\,\dot{\bar{e}}_p & ;if\ \bar{e}_i < \bar{e}_p \leq \bar{e}_c \\ \dfrac{(1-d_c)^{\beta_d}}{\bar{e}_c - \bar{e}_0}\,\dot{\bar{e}}_p & ;if\ \bar{e}_c < \bar{e}_p \end{cases} \tag{10}$$

According to Equation (10), $\bar{e}_0$ is the effective plastic strain at the initial damage state (threshold effective plastic strain), $\bar{e}_i$ is an effective plastic strain within the range $[\bar{e}_0{:}\bar{e}_c]$ (used to describe a bilinear damage function), $\bar{e}_c$ is the critical effective plastic strain (i.e., the plastic strain at fracture), d_i is the damage at $\bar{e}_i$ level, d_c is the critical damage, and β_d is a numerical parameter to describe the damage acceleration once the critical damage is reached and represents the final damage evolution up to the physical rupture of the specimen. Notice that the values of $\bar{e}_0$, $\bar{e}_i$, $\bar{e}_c$, d_i and d_c are material parameters to be characterized from the experiments. In this case, the damage index is defined as $I = d/d_c$, where its average value is also computed using Equation (6).

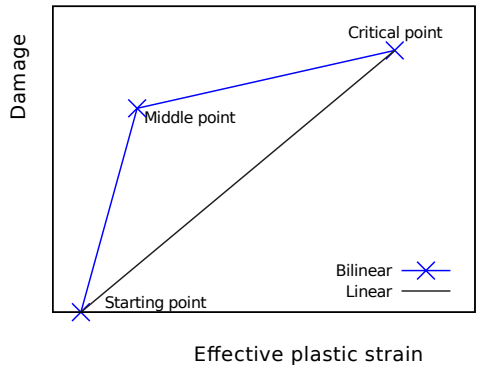

Figure 4. Simple sketch of damage paths. Different linear and bilinear damage evolutions can be obtained using different starting, middle, and critical points. Those points need to be determined by damage characterization for a given material.

2.4. Hardening Model

The hardening model used to fit the mechanical behavior of the material corresponds to the modified Voce model:

$$\bar{\sigma} = \bar{\sigma}_0 + h\bar{e}_p + Q\left[1 - \exp\left(-b\,\bar{e}_p\right)\right] \tag{11}$$

where $\bar{\sigma}_0$, h, Q, and b correspond to parameters that depend on the material and must be characterized from experimental results. The parameter calibration procedure is carried out via a standard least-squares approach aimed at minimizing the error between the numerical predictions and the corresponding experimental measurements.

The same hardening model is used in both damage approaches, but in the case of the coupled model, the equivalent stress is affected by the damage through the relation $(1 - d)$. Consequently, even though the same model is used, the response in the coupled case is different because when the damage begins to evolve, the hardening is affected by that value, creating a difference with the uncoupled case, where the hardening is not affected by the obtained damage. This also implies that the characterization of the hardening model must be carried out for each damage model approach studied since the values obtained for the parameters using uncoupled criteria will not be the same as those obtained when using the coupled damage criterion.

2.5. Fem Analysis

Numerical simulation of the tensile tests was carried out by means of an 'in-house' finite element code that contains in its libraries the plasticity and damage equations that allow this analysis to be carried out. The cylindrical specimen was represented in a two-dimensional simplification, assuming axisymmetry. Half of the SRB sample was discretized with a height of 12 mm (half of the initial extensometer length) and a radius of 3.0 mm at the top. As already mentioned, a small linear radius variation along the bar length was considered in order to trigger the necking formation in the middle of the specimen (i.e., the radius at the symmetry plane is 2.97 mm). A mesh composed of 1248 four-noded isoparametric elements (1330 nodes) was used in SRB specimens. The same type of elements was used in the spatial discretization of the notched specimens: 1711 elements (1808 nodes) were used in NRB R8 and 1633 elements (1728 nodes) were used in NRB R2.8). The four-Gauss-point integration rule is used, including a B-bar technique described by Celentano [62] to avoid volumetric locking. An axial displacement was applied to the upper boundary of each specimen, according to the speed at which the experimental tests were carried out, up to a value corresponding to the average fracture elongation observed in the experiments. A higher density of elements was considered in the notched area to better capture the distribution of internal variables in that region. The meshes used in this work for each geometry are presented in Figure 5. The mesh convergence was evaluated (results not shown) based on effective plastic strain values and the main internal variables considered in the different damage models (von Mises stress, maximum principal stress, hydrostatic stress, among others), concluding that finer meshes do not substantially modify damage results. The approach in this work treats damage as a continuous variable and does not aim to numerically reproduce the discontinuity of fracture, but rather to predict the conditions under which fracture is expected to develop. For this reason, it can be concluded that element size is not a critical factor. However, mesh convergence was performed to validate the numerical results presented in this work.

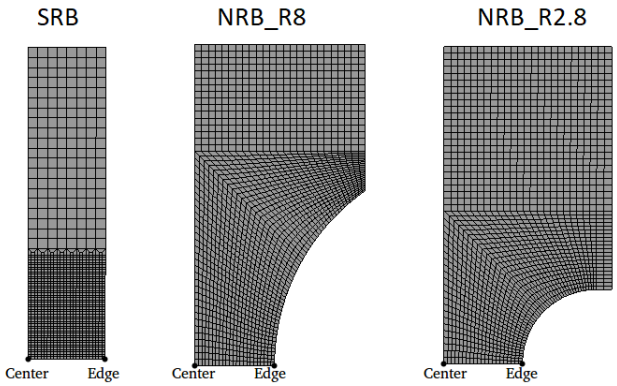

Figure 5. FEM discretization: meshes composed of four-noded isoparametric elements are used to describe smoothed round bars (SRB) and notched round bars (NRB). Note: the indicated center (at the axisymmetric axis) and edge points (at the specimen radius) were used in the analyses.

3. Experimental and Numerical Results

Experimental and numerical results are reported in the present section. Hardening and damage responses using uncoupled and coupled damage models are presented. In particular, the discussion is focused on the comparison between experimental data and numerical predictions. Differences in the results obtained with the uncoupled and coupled models are pointed out. The analysis is specifically made considering the triaxiality evolution during damage analyses. The main goals of this section are to calibrate the parameters of the models and to validate them in triaxial conditions through the analysis of the notched specimens.

3.1. Experimental Results

Experimental results were obtained after performing tensile tests on the SRB and NRB specimens, each of them tested three times. The elongation (relative to an initial gauge length of 24 mm) was recorded by digital image correlation (DIC), while the load was registered using a load cell attached to the universal testing machine. Through data post-processing, the recorded experimental signals were synchronized to obtain the stress–strain curves for both SRB and NRB specimens. A summary of the experimental results in terms of the engineering strain stress curve is shown in Figure 6. The effect of the notch on the mechanical response of the material is evident, as there is a noticeable increase in tensile strength accompanied by a significant decrease in ductility. Specifically, the fracture strain for the SRB case is 20.12%, while for the NRB R8 case it is 3.26 and for the NRB R2.8 case it is 2.05%.

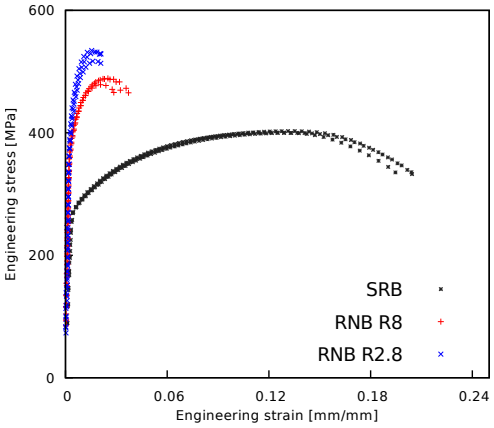

Figure 6. The obtained experimental engineering strain–stress curves of SRB and NRB specimens exhibit the effect of the notch reduction: an increase in tensile strength is observed with decreasing failure strains, denoting a high decrease in ductility.

The effect of the notch radius on the fracture mechanism was also investigated. Scanning Electron Microscopy (SEM) observations were performed on longitudinal sections of the fractured samples. Figure 7 depicts the fracture profiles at low magnifications for the three tested specimen configurations. Although there are slight differences between the fracture profiles, all of them seem to be ductile from a macroscopic point of view. It is evident the development of a "cup and cone" fracture, that is, an approximately flat zone at the center and the presence of shear lips in the edge.

More detailed SEM observations at higher magnifications of the three fracture surfaces, corresponding to the original SRB specimen and the notched specimens NRB R8 and NRB R2.8, reveal patterns related to fracture mechanisms of the samples. In the case of the SRB specimen, which experienced greater plastic macroscopic deformation, the observations shown in Figure 8a indicate a predominantly ductile fracture mechanism (nucleation, growth, and coalescence of microcavities) due to the presence of the dimples typically found in this kind of fracture mechanism. The deformation of the matrix around the non-metallic inclusions (some of them indicated with red arrows in Figure 8) is evident, with fewer regions showing cleavage planes (transgranular brittle fracture, indicated with blue arrows) surrounding the characteristic dimples.

In contrast, the notched specimens, especially NRB R2.8—see Figure 8c—exhibit a significant reduction in the presence of dimples and an apparent transition towards a more brittle cleavage fracture. This suggests that the reduction in the notch radius is associated with a decrease in both fracture deformation and material ductility. The NRB R8 specimen—see Figure 8b—while displaying intermediate characteristics between SRB and NRB R2.8, closely resembles the SRB specimen in terms of ductility.

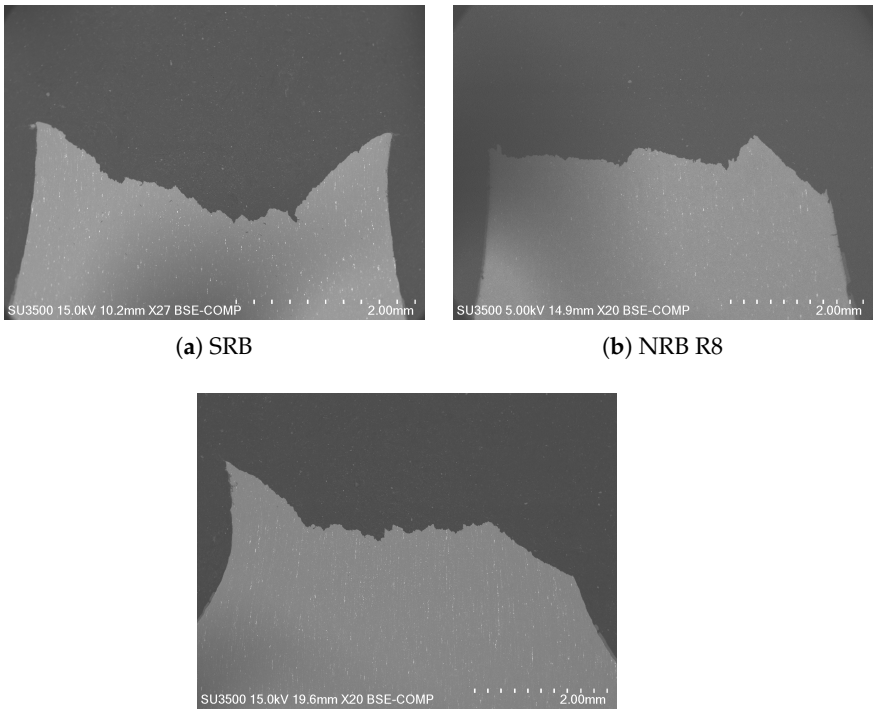

(**a**) SRB (**b**) NRB R8

(**c**) NRB R2.8

Figure 7. Fracture profile for (**a**) SRB, (**b**) NRB R8, and (**c**) NRB R2.8.

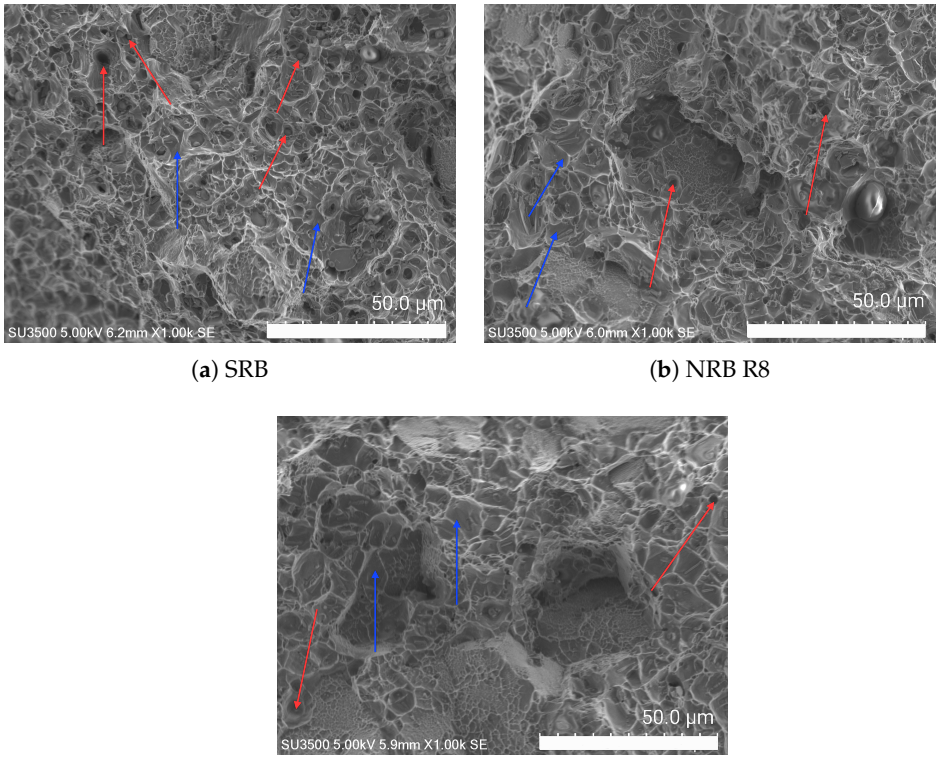

(**a**) SRB (**b**) NRB R8

(**c**) NRB R2.8

Figure 8. SEM observations of fracture surfaces for (**a**) SRB, (**b**) NRB R8, and (**c**) NRB R2.8.

Overall, the three specimens were fractured by a combination of transgranular ductile and cleavage brittle mechanisms, but in different proportions. These findings support the hypothesis that the notch radius significantly influences the fracture behavior of materials,

with a reduction in radius leading to reduced fracture deformation and ductility, while greater fracture deformation is associated with predominantly ductile fracture behavior.

3.2. Uncoupled Damage Analysis

In this subsection, results and discussion are made based on uncoupled damage models (see Table 1). Firstly, the material hardening parameters are adjusted based on the experimental results obtained for the smoothed (SRB) specimen. Secondly, the quality of the fit is verified on the notched specimens (NRB R8 and NRB R2.8). Then, the critical parameters of each uncoupled damage model are obtained using numerical simulations and finally, the damage index in the fracture strain stage is calculated to evaluate the fracture predictive capability of each uncoupled model.

3.2.1. Hardening Response

Numerical results of the engineering curve obtained after simulating the tensile test with the parameters of the modified Voce model (see Equation (11)) defined in Table 2 (obtained by applying the fitting method described in Section 2.4 to the experimental data collected in this study) are presented in Figure 9a for the SRB specimens, and are validated in Figure 9b for the NRB R8 specimens and Figure 9c for the specimens NRB R2.8. These results do not consider the coupling of the damage in the mechanical response of the material, so they are considered uncoupled.

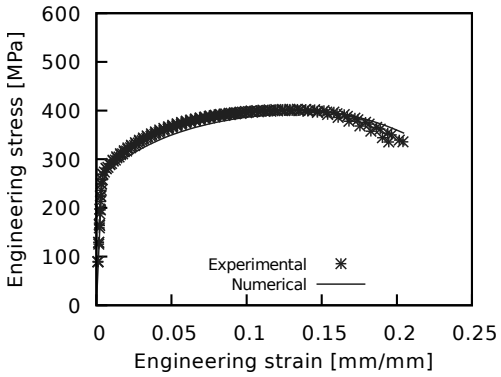

(**a**) SRB

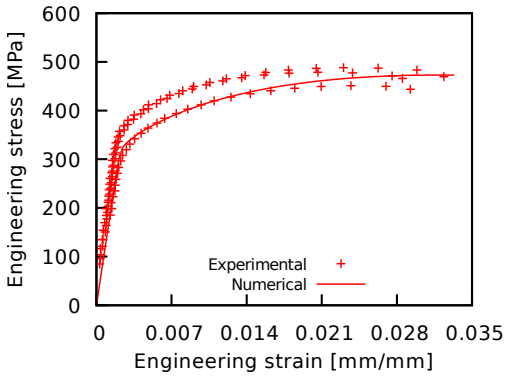

(**b**) NRB R8

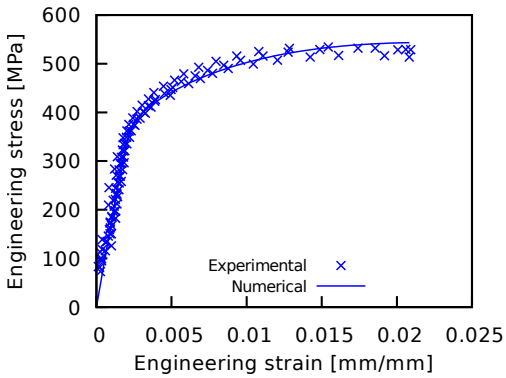

(**c**) NRB R2.8

Figure 9. Numerical versus experimental tensile test curves. Material hardening parameters are obtained by adjusting the numerical uncoupled hardening response with the experiments for SRB (**a**), and the quality of such parameters is verified by comparison of the computed hardening responses for notched specimens with the experimental curves in NRB R8 (**b**) and NRB R2.8 (**c**).

Table 2. Uncoupled hardening parameters obtained by fitting the numerical uncoupled hardening response for SRB specimens with the experimental data.

Parameter	$\bar{\sigma}_0$	h	Q	b
Value	265.9 MPa	118.0 MPa	202.4 MPa	14.2

3.2.2. Damage Models Characterization Using the Smoothed Round Bar

Characterization of the critical damage value for each of the uncoupled models presented in Section 2.3.1 of this work was carried out numerically using the experimental data of the SRB specimen. Damage must be evaluated at the instant in which the experimental fracture deformation is numerically reached, to obtain the critical constants of each uncoupled model. Table 3 shows the results for the damage obtained according to each model both in the center and on the edge (see the first mesh of Figure 5) of the specimen, always considering its critical zone, i.e., the symmetry plane. Additionally, the area-weighted average damage value (according to Equation (6)) is given, which is considered as the critical damage value. The parameters of the González et al. model [53] (Equation (5)) used in the simulations that correctly reproduce the experimental results presented in this work are $\alpha = 0.15$ and $\beta = 1.90$.

Table 3. Critical damage values computed for uncoupled models. Note that damage localizes at the center of the specimens. The average (i.e., the area-weighted average damage value from Equation (6)) is adopted as the critical damage value for each model.

Model	**Center**	**Edge**	**Average**
Rice and Tracey	0.283	0.185	0.218
Chaouadi (modified) [MPa]	512.3	289.7	363.9
Ayada et al.	0.226	0.126	0.160
González et al.	0.093	0.033	0.053

3.2.3. Damage Evaluation in Notched Bars

The spatial distribution of the damage index reached by each model at the moment when the numerical simulation achieved the experimental fracture strain reported for the NRB R8 specimen is presented in Figure 10. The same analysis is presented for the NRB R2.8 specimen in Figure 11. This damage index is calculated according to Equation (1) and represents the ratio between the damage value reached by each model and the critical damage previously presented in Table 3. Therefore, the average damage index is expected to be equal to one at the instant of fracture. In Figures 10 and 11, areas with a damage index greater than one are highlighted in black. Additionally, the evolution of the damage index at points of interest (center and edge), as well as the weighted average (according to Equation (6)), are shown in Figure 12.

According to the results presented in Figures 10 and 11, the four uncoupled damage models always concentrate the maximum values in the center of the studied specimens, since that is where a greater evolution of the mean stress takes place and therefore a greater evolution of triaxiality. In addition, the center of the specimens develops a higher level of effective strain compared to the values reached on the edge. Table 4 shows the detail of the damage index obtained in the center and on the edge of the specimens. The weighted average damage index (see Equation (6)) predicted by each model for both of the notched specimens is also presented in Table 4. According to the values presented in this table, a unit damage index is not obtained when the weighted average damage criterion is used for all the uncoupled models analyzed. However, the González et al. model is the only one of the four models that is able to predict damage index greater than the unit value in the center of both notched specimens, as presented in Figures 10 and 11. A physical interpretation of these results is that, although the specimen has not yet fully fractured as

occurred experimentally, the González et al. model predicts that the critical condition has already been reached at the center of both specimens.

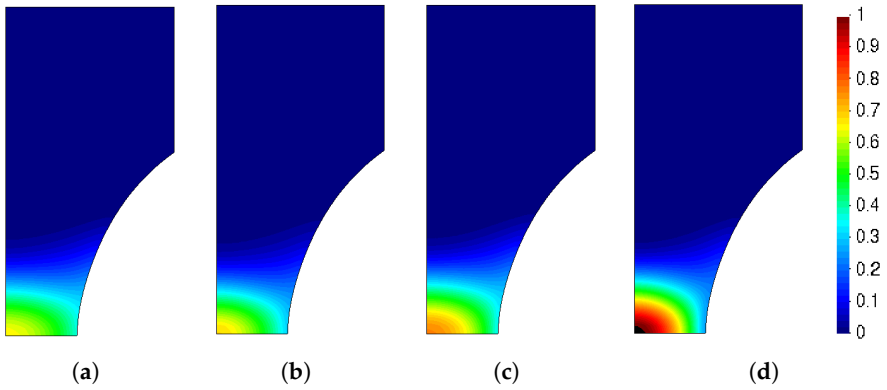

Figure 10. Damage index distribution in NRB R8 for uncoupled models at a fracture strain of 3.26%: (**a**) Rice and Tracey, (**b**) Chaouadi (modified), (**c**) Ayada et al., and (**d**) González et al.

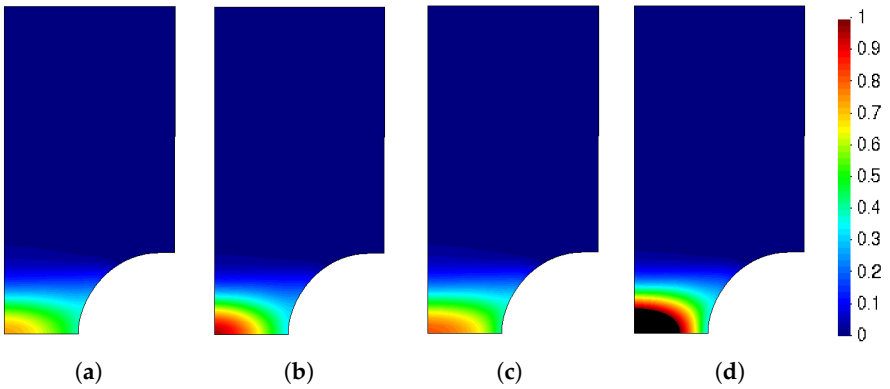

Figure 11. Damage index distribution in NRB R2.8 for uncoupled models at a fracture strain of 2.05%: (**a**) Rice and Tracey, (**b**) Chaouadi (modified), (**c**) Ayada et al., and (**d**) González et al.

Table 4. Center, edge, and weighted average damage index for uncoupled models. Total failure is reached when a unit average damage index is computed. According to these results, all models fail to describe the rupture using this criterion. Nevertheless, the model proposed by González et al. can properly describe the initiation of damage as values index higher than one are obtained from the center and along the radius of the specimens.

	NRB R8			NRB R2.8		
Model	**Center**	**Edge**	**Average**	**Center**	**Edge**	**Average**
Rice and Tracey	0.6509	0.3721	0.465	0.7353	0.4008	0.512
Chaouadi (modified)	0.6812	0.3104	0.434	0.9561	0.3435	0.547
Ayada et al.	0.7656	0.3560	0.492	0.8134	0.4176	0.549
González et al.	1.0261	0.2611	0.516	1.4927	0.3566	0.735

3.3. Coupled Damage Analysis

In this subsection, results and discussion are provided based on a recently proposed bilinear extension (see Equation (10)) of the coupled Lemaitre damage model. For the coupled analysis, the damage parameters of the material are firstly adjusted, and then the original hardening parameters of the modified Voce model (those obtained in the uncoupled analysis) are readjusted because the evolution of the damage affects the constitutive relationship of the material when coupled models are used. Finally, the damage index in the fracture strain stage is calculated for notched specimens in order to evaluate the fracture-predictive capability of this bilinear coupled model.

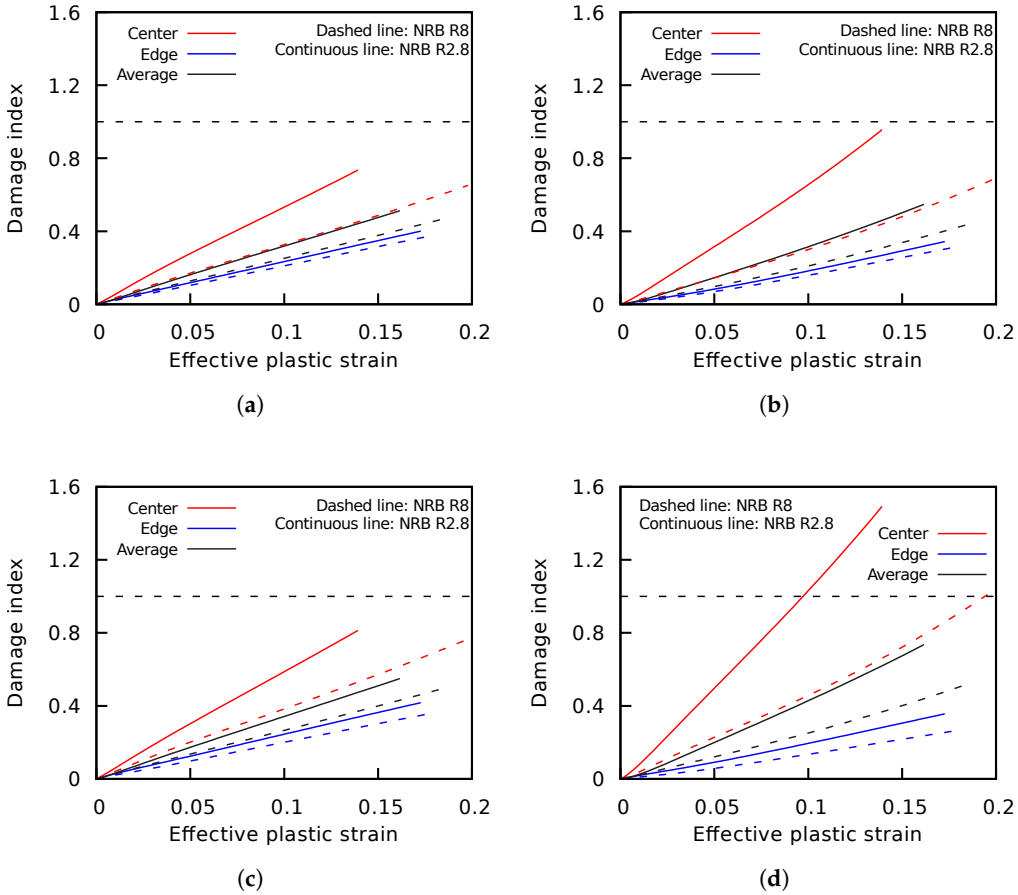

Figure 12. Damage index (center, edge, and average) vs. effective plastic strain curves for uncoupled models in notched specimens. The slopes of these curves help to understand the model's behavior. Steep slopes denote high damage evolution for a given effective plastic strain, and, as the models are uncoupled, this fact directly shows the capacity in the damage prediction. For all models, the damage increases when the notch radius decreases. In addition, high slopes are described by model (**d**), in agreement with its effective description of the damage. Notice that only a linear damage path can be described in this context. (**a**) Rice and Tracey, (**b**) Chaouadi (modified), (**c**) Ayada et al., and (**d**) González et al.

3.3.1. Damage Characterization

The characterization of the coupled Lemaitre model is performed through experimental loading and unloading tensile tests for the 2024 aluminum alloy studied in this work. The calculated damage is obtained by evaluating the loss of rigidity of the material when subjected to cyclic loading and unloading loads. A decrease in the elastic modulus in each of the unloading carried out is observed, as a result of the damage. The experimental data obtained a fit with the bilinear model recently proposed by the authors [58] and presented earlier in Section 2.3.2. The result of the fit is presented in Figure 13, and Table 5 summarizes the parameters of the bilinear model (see Equation (10)) considered in the characterization of the damage.

Table 5. Coupled damage parameters (see Figure 4 and Equation (10)) for the Al-2024 aluminum alloy obtained by fitting the bilinear model with experimental values.

$\bar{e}_0$	$\bar{e}_i$	d_i	$\bar{e}_c$	d_c	β_d
0.001	0.07	0.24	0.31	0.28	1.50

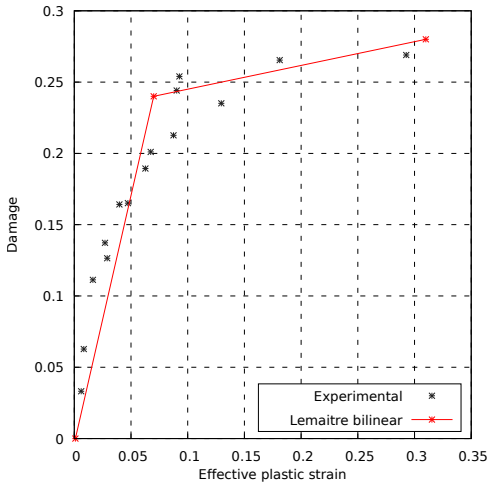

Figure 13. Coupled damage characterization: the experimental data obtained are fitted using a bilinear damage path by minimizing the root mean square of the error between experiments and model. See the obtained values of the characteristics in Table 5.

3.3.2. Damaged Hardening Response

When considering the coupled Lemaitre model with the bilinear evolution of the damage, the parameters of the hardening model must be readjusted since the damage affects the constitutive relationship of the material. The new adjustment of these parameters is performed on the SRB specimen, and then the quality of the fit is verified on the notched specimens (NRB R8 and NRB R2.8). The new parameters of the modified Voce hardening model are summarized in Table 6. Note that only the Q and b parameters were modified with respect to the previous values defined in Table 2 and used in the uncoupled characterization ($\bar{\sigma}_0$ and h have not been modified). The numerical results obtained when modeling the traction in the studied specimens are presented in Figure 14a for the SRB specimens, Figure 14b for the NRB R8 specimens, and Figure 14c for the NRB R2.8 specimens. The results presented in these figures show a good fit of the numerical curves after readjusting the hardening parameters and coupling the Lemaitre model with a bilinear damage evolution.

Table 6. Coupled hardening parameters of the modified Voce model using Lemaitre model with the bilinear damage path.

Parameter	$\bar{\sigma}_0$	h	Q	b
Value	265.9 MPa	118.0 MPa	264.6 MPa	11.3

3.3.3. Damage Evaluation in Notched Bars

Figure 15 shows the damage index contours calculated with the coupled Lemaitre model using the bilinear extension characterized from the damage curve presented in Figure 13, and its evolution is presented in Figure 16. With the damage evolution curve, the prediction of damage calculated with the Lemaitre model does not reproduce the fracture of the notched specimens. A sensitive analysis of the parameters involved, i.e., effective plastic strain at fracture and the critical damage value, was performed to assess their influence on the results when the Lemaitre coupled model is used. From these analyses, small changes in such variables could promote more accurate results for the studied coupled model. Nevertheless, such improvements are not significant in the present context. However, it is not correct to rule out the use of this model; rather, one must highlight the importance of a correct characterization of the damage evolution in the material under study. On the other hand, it is important to remark that the radial distribution of the damage calculated with

the Lemaitre model is much more homogeneous in the cross-section of the specimen than the damage distribution obtained with the uncoupled models (which tends to be strongly located at the center of the specimen).

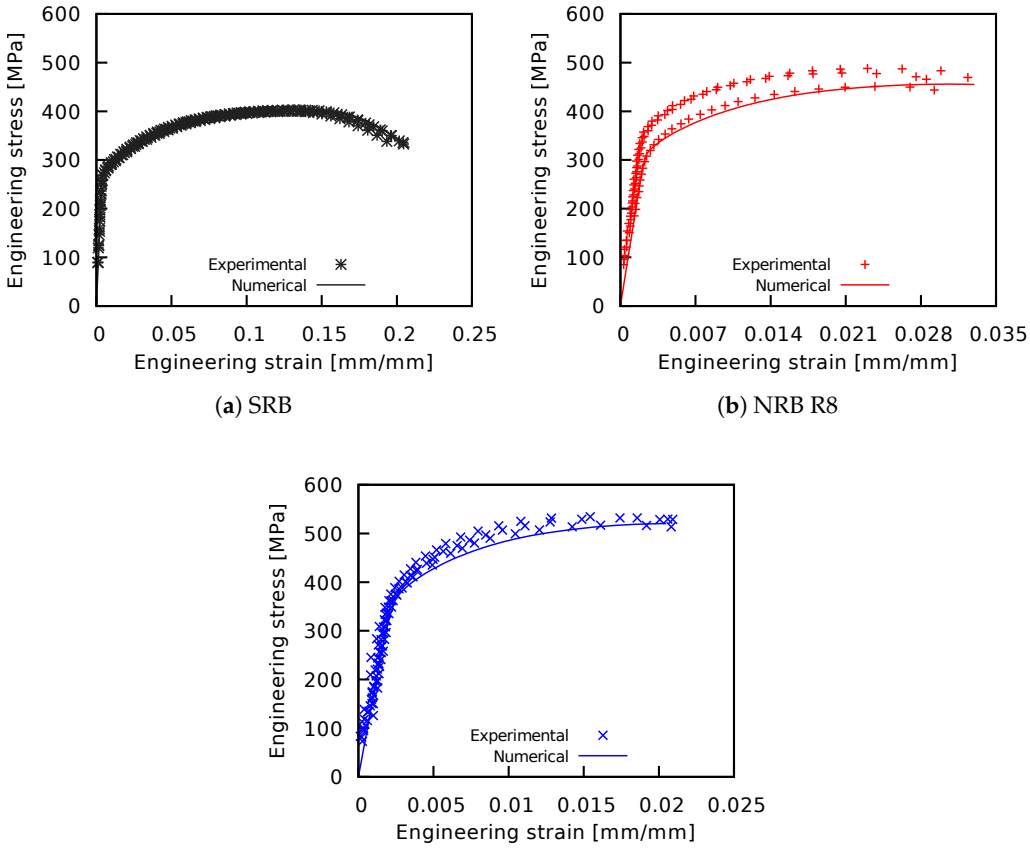

(**a**) SRB

(**b**) NRB R8

(**c**) NRB R2.8

Figure 14. Numerical versus experimental tensile test curves. Coupled hardening response for (**a**) SRB, (**b**) NRB R8, and (**c**) NRB R2.8 computed with the coupled material hardening parameters obtained from calibration numerical results with experimental data for SRB, showing that they produce the simultaneous best fit for all the specimens.

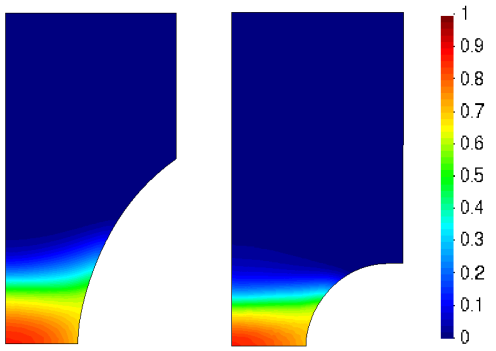

(**a**) (**b**)

Figure 15. Damage index distribution with the coupled model for (**a**) NRB R8 and (**b**) NRB R2.8. The damage index distribution is more homogeneous along the radius than those reported for uncoupled models, which may mean that the coupled model can succeed in describing the initiation of the simultaneous rupture over the entire radius. Nevertheless, the predicted damage index is far from the unit value in comparison with the results computed with the uncoupled Gonzalez's model.

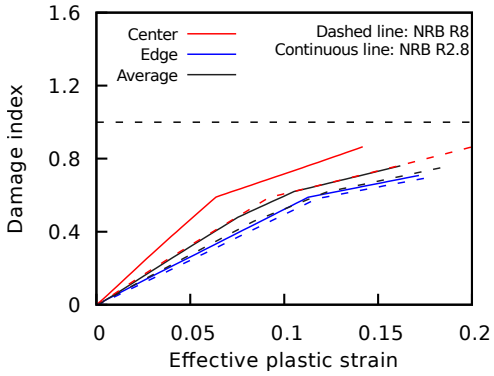

Figure 16. Damage index (center, edge, and average) vs. effective plastic strain curves for the coupled model in notched specimens. The present figure plots the computed damage index where the bilinear trend is clearly observed. For a given effective plastic strain, a high damage index is obtained for notched specimens with a lower notch radius.

3.4. Triaxiality Evolution

Each of the damage models analyzed above has an explicit dependence in its formulation on triaxiality. However, not all are able to correctly predict the fracture in conditions other than the uniaxial case. On the other hand, effective plastic strain plays an important role in the development of ductile fracture. The analysis presented below seeks to relate both variables, studying the evolution of triaxiality as a function of the effective plastic strain both in the center and on the edge of each specimen. The analysis is performed for the SRB and both NRB specimens at the center (Figure 17a) and at the edge (Figure 17b), evaluating the maximum value in both cases. Additionally, Figure 18 summarizes the maximum values of triaxiality and plastic strain (both weighted across the cross-section, consistent with the same formulation proposed to weight the damage index in Equation (6)) for the three cases studied, at the time of the fracture using uncoupled and coupled approaches. In this figure, it can be seen that the fracture strain decreases strongly when the triaxiality increases.

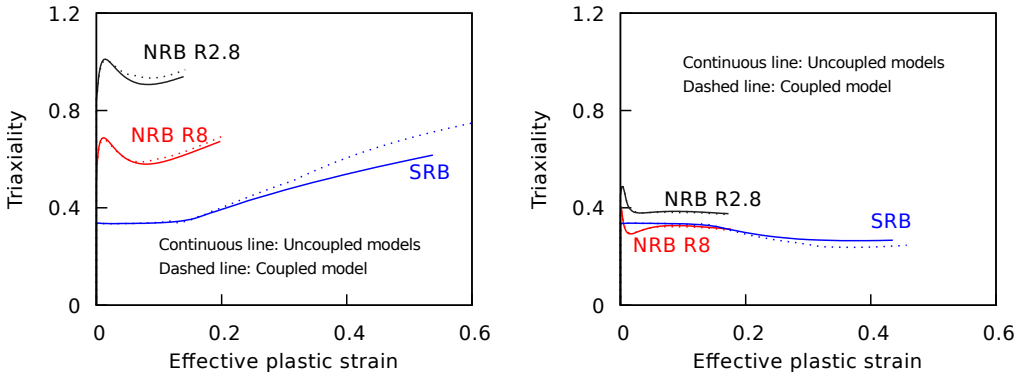

(**a**) Center (**b**) Edge

Figure 17. Triaxiality versus effective plastic strain curves. Comparison between uncoupled and coupled models for smoothed (SRB) and notched specimens (NRB) computed at the center (**a**) and edge (**b**) points. Higher triaxiality values are developed when reducing the notch radius; this fact is relevant at the center of the specimen.

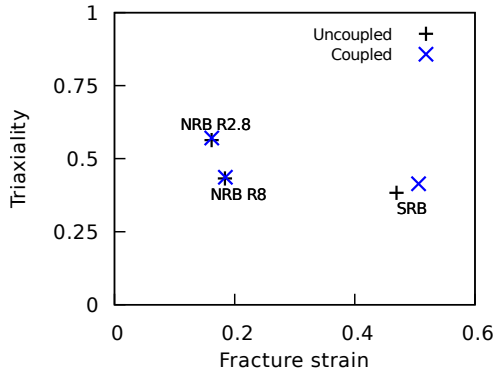

Figure 18. Maximum triaxiality and strain (both averaged) at fracture. Uncoupled and coupled models exhibit similar trends, decreasing the fracture strain when triaxiality increases.

An analysis of the radial distribution of the mean stress and the equivalent von Mises stress for the central cross-section of the specimen when fracture strain was reached is presented in Figure 19, both for the uncoupled models and for the coupled model. The radial direction has been normalized as a function of the radius of the specimen: 0 is the center and 1 is the edge of the specimen. Both variables (i.e., mean stress and the equivalent von Mises stress) play an important role in the evolution of triaxiality. The radial distribution of the equivalent von Mises stress is rather homogeneous, while the mean stress presents higher levels in the center than in the edge, which is why higher levels of triaxiality are reached in the center of the specimen. No great differences are observed in the results obtained in the notched specimens using the uncoupled or coupled models, but not in the SRB specimen, where both the mean stress and the von Mises stress present different values with the coupled model than with the uncoupled models.

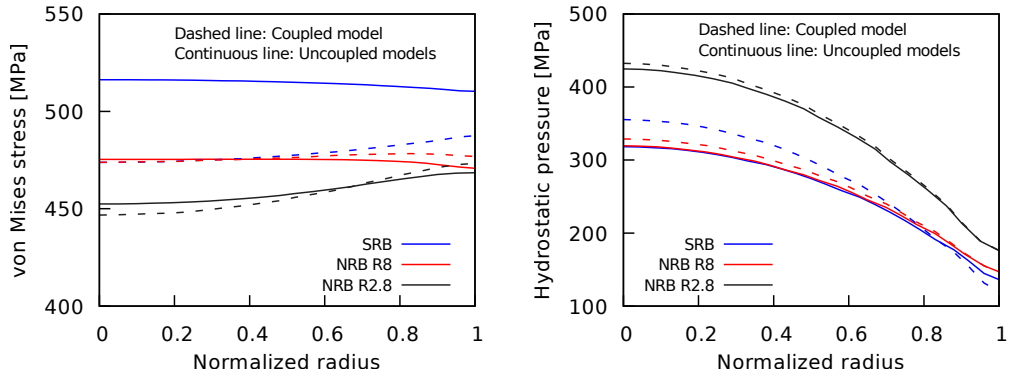

Figure 19. Normalized radial distribution of the equivalent von Mises stress (**a**) and mean stress (**b**) in the cross-section of the specimens at the fracture stage. The von Mises stress has a practically constant distribution along the radius and the mean stress substantially varies from the center to the edge of the specimen. These trends justify the high triaxiality at the center of the specimen, and the strong dependence of the evolution of triaxiality on mean stress.

4. Discussion

This section points out the main aspects derived from the experimental and numerical work reported in previous sections, as well as its relationship with other published studies. The discussion is mainly related to three aspects. First, the results of the tests are discussed, which constitute the experimental evidence that supports the development of this work. Second, numerical aspects of determining the parameters of the damage and hardening model are discussed. Finally, the discussion focuses on the incidence of triaxiality in the

damage evolution and the differences between the results of uncoupled and Lemaitre coupled models using a bilinear damage path.

4.1. Experimental Results

The effect of the notch on the mechanical response of the material can be observed from the tensile test results reported in Figure 6. The three types of specimens used in this work have the same resistive diameter, so the differences in their behavior are mainly due to the effect of the notch, which is reflected in triaxiality. The smoothed specimen exhibits ductile behavior, while the notched specimens tend to exhibit less ductile behavior, as evidenced by a strong decrease in fracture strain (5 mm, 0.8 mm, and 0.5 mm average elongation before fracture for SRB, NRB R8, and NRB R2.8 respectively). The experimental results reported in this work correctly agree with the trend reported in other works, in relation to the effect of the notch on the mechanical behavior in this type of material (e.g., the results reported by Li et al. [34], Zhang et al. [33] or Bao and Wierzbicki [36] in tensile tests of notched specimens of aluminum alloys).

The transition from ductile to less ductile behavior observed in the notched specimens can be linked to the SEM observations discussed earlier, where reduced dimple formation and increased cleavage fractures were evident with smaller notch radii, i.e., greater triaxialities. This correlation underscores the importance of geometric factors, such as the notch radius, in influencing fracture behavior and provides valuable insights for the design and analysis of materials under different loading conditions.

4.2. Damage and Hardening Parameters

The characterization of the uncoupled damage models is classically carried out through numerical simulations based on the experimental results of the monotonic axial tensile tests: the damage value obtained upon reaching the fracture elongation is considered as the critical damage value. However, the characterization of coupled models is more complex, since even the simplest version of Lemaitre's model (the one that considers a linear evolution of damage with respect to plastic strain) requires not only critical damage but also at least two more parameters. The type of test that is classically used to characterize this type of model is the cyclic load–unload tensile test since it allows the accumulation of permanent strain in the material, and by means of the degradation of Young's modulus, the damage evolution can be determined. In this work, the experimental characterization of the damage carried out for the aluminum alloy 2024 was used, and from these results, the bilinear extension of the Lemaitre model was adjusted. The characterization carried out in this work shows that in this type of aluminum alloy, the damage evolves strongly at the beginning of the plastic range, and subsequently, its rate of evolution decreases. This inflection point corresponds to the intermediate point where the bilinear model changes its slope. On the other hand, the hardening parameters used in conjunction with the uncoupled damage models (see Table 2) must be readjusted when coupled damage models are used (see Table 6) since in this case, the mechanical response of the material is affected by the damage and a readjustment of the hardening parameters is required for a correct description of the behavior of the material. The numerical results obtained in the notched specimens allow the validation of this readjustment of parameters since after readjusting the parameters and coupling the damage, the numerical results of the notched specimens show a good agreement with the experimental results. Both characterizations (hardening and damage parameters), must be carefully analyzed. The incidence of one set of parameters over the other (for example, the incidence of damage parameters over hardening parameters) is a topic that has not yet been explored in depth.

4.3. Triaxiality and Damage

The effect of the notch on the evolution of triaxiality has been verified: there is an increase in triaxiality stress when the notch radius decreases, due to an increase in mean

stress. This trend agrees with the results presented by Bao and Wierzbicki [36] in terms of the average stress triaxiality proposed in their work.

Two approaches to damage have been studied in this work. The main difference between them is that in the coupled models, the evolution of the damage affects the constitutive relationship of the material, and therefore, the evolution of the internal variables is also affected. This is why the prediction of the evolution of triaxiality is not exactly the same between both model's approaches. Both approaches reproduce in a good way the increase in triaxiality due to the notch in the specimens, but they fail to correctly predict the fracture strain, or in other words, they do not reach the unit value for the damage index when the simulation reaches fracture strain.

The different slopes of the curves relating damage index with effective plastic strain (see Figures 12 and 16) are a direct consequence of the different triaxialities developed in the specimens, as damage depends on triaxiality according to Equations (2)–(5) for uncoupled models and Equations (7)–(9) for the Lemaitre coupled model. Nevertheless, all the models can predict increased damage in the center of the specimens and estimate a higher damage evolution when the notch radius decreases. These aspects are related to the higher mean stress values developed at the center of the specimens and are consistent with the model's assumptions.

There is a difference between a local criterion to predict the initiation of the fracture, mainly associated with a microscopic approach to the fracture, and a global criterion to predict the total fracture of the specimen, associated with a macroscopic approach. The local criterion is based on the analysis of the damage calculated at the nodal level and determines that the beginning of the fracture starts when any node exceeds the critical damage value. The global criterion, on the other hand, predicts that the total fracture of the specimen is reached when the weighted average damage value in the critical cross-section (the one located in the geometric center of the specimen and where the deformation is located) exceeds the critical damage value selected under the same criterion. According to the macroscopic approach used in this work, none of the studied models achieves the correct reproduction of the fracture phenomenon. However, the model of Gonzalez et al. [53] predicts fracture initiation in both notched specimens when the local approach is considered.

5. Conclusions

The main objective of this work was to study the predictive capacity of fracture that different damage models have under positive triaxialities greater than those achieved in uniaxial tensile tests. To this end, tensile tests were carried out on cylindrical and notched specimens. Uncoupled damage models and a coupled Lemaitre model with the recently proposed bilinear extension [58] were characterized in this work using the results of cylindrical specimens and tested under triaxial conditions other than uniaxiality using the results obtained in the notched specimens.

In addition, the incidence of triaxiality on fracture strain was verified in experimental results, with an inverse relationship. The numerical results have shown a good agreement with this trend, demonstrating the strong incidence of triaxiality in the development of the damage.

The presented uncoupled models relate the damage with the triaxiality; however, not all of them satisfactorily predict the fracture experimental data. Although none of the models achieved a correct approximation of the fracture in the notched specimens, the uncoupled model proposed by González et al. [53] was the only one that predicted the critical damage, since in its formulation it potentially considers the effect of effective plastic strain and triaxiality. The coupled Lemaitre model with the bilinear extension presents trends similar to the results obtained by the uncoupled damage models. However, the critical condition in the notched specimens computed with such a model is slightly underestimated. The limitations of the uncoupled models include their inability to account for the feedback effect of damage on material hardening, leading to potential underestimations of damage evolution at higher strain levels. However, these models offer simplicity and

reduced computational costs. In contrast, the coupled models, while more computationally demanding, provide a more accurate representation of the interaction between damage and material hardening, particularly in the later stages of strain.

In addition to the comprehensive analysis previously presented, it is worth noting the remarkable coherence observed between the macroscopic experimental results obtained from tensile tests and the microscopic findings derived from SEM analysis, as well as the numerical simulations. These results collectively reinforce the significant influence of triaxiality on fracture behavior, demonstrating a consistent inverse relationship between triaxiality and fracture strain. This alignment between macroscopic, microscopic, and numerical outcomes underscores the robustness and reliability of the findings, providing valuable insights into the complex interplay of factors affecting material fracture under varying loading conditions.

Author Contributions: Conceptualization, Á.G., D.C. and M.C.; methodology, Á.G., D.C. and M.C.; software, Á.G. and D.C.; validation, Á.G., D.C., M.C. and J.-P.P.; formal analysis, Á.G., D.C., M.C. and J.-P.P.; investigation, Á.G.; resources, D.C.; data curation, Á.G.; writing—original draft preparation, Á.G.; writing—review and editing, Á.G., D.C., M.C. and J.-P.P.; visualization, Á.G.; supervision, D.C. and M.C.; project administration, D.C.; funding acquisition, D.C. All authors have read and agreed to the published version of the manuscript.

Funding: This research was financially supported by the Chilean Agency of Research and Development (ANID) through Fondecyt Project 1220211 and the Wallonie Bruxelles International collaboration project No. 5.

Data Availability Statement: The original contributions presented in the study are included in the article, further inquiries can be directed to the corresponding author.

Acknowledgments: The support provided by the National Agency of Research and Development ANID through FONDECYT Project No. 1220211; the Wallonie Bruxelles International collaboration project No. 5; and the Dirección de Investigación y Desarrollo Tecnológico (DICYT) Vicerrectoría de Investigación, Innovación y Creación (VRIIC-Ex VRIDEI) at Universidad de Santiago de Chile (USACH); is gratefully acknowledged.

Conflicts of Interest: The authors declare no conflicts of interest.

References

1. McClintock, F. A criterion for ductile fracture by the growth of holes. *J. Appl. Mech.* **1968**, *35*, 363–371. [CrossRef]
2. Lemaitre, J. A continuous damage mechanics model for ductile fracture. *J. Eng. Mater. Technol.* **1985**, *107*, 83–89. [CrossRef]
3. Gurson, A.L. Continuum theory of ductile rupture by void nucleation and growth: Part I—yield criteria and flow rules for porous ductile media. *J. Eng. Mater. Technol.* **1977**, *99*, 2–15. [CrossRef]
4. Rice, J.R.; Tracey, D.M. On the ductile enlargement of voids in triaxial stress field. *J. Mech. Phys. Solids* **1969**, *17*, 201–217. [CrossRef]
5. Ganjiani, M. A damage model for predicting ductile fracture with considering the dependency on stress triaxiality and Lode angle. *Eur. J. Mech. Solids* **2020**, *84*, 104048. [CrossRef]
6. Hancock, J.; Mackenzie, A. On the mechanisms of ductile failure in high-strength steels subjected to multi-axial stress-states. *J. Mech. Phys. Solids* **1976**, *24*, 147–160. [CrossRef]
7. Dunand, M.; Mohr, D. On the predictive capabilities of the shear modified Gurson and the modified Mohr–Coulomb fracture models over a wide range of stress triaxialities and Lode angles. *J. Mech. Phys. Solids* **2011**, *59*, 1374–1394. [CrossRef]
8. Achouri, M.; Germain, G.; Dal Santo, P.; Saidane, D. Experimental characterization and numerical modeling of micromechanical damage under different stress states. *Mater. Des.* **2013**, *50*, 207–222. [CrossRef]
9. Gholipour, H.; Biglari, F.; Nikbin, K. Experimental and numerical investigation of ductile fracture using GTN damage model on in-situ tensile tests. *Int. J. Mech. Sci.* **2019**, *164*, 105170. [CrossRef]
10. Bonora, N.; Gentile, D.; Pirondi, A.; Newaz, G. Ductile damage evolution under triaxial state of stress: Theory and experiments. *Int. J. Plast.* **2005**, *21*, 981–1007. [CrossRef]
11. Peng, J.; Wang, Y.; Dai, Q.; Liu, X.; Liu, L.; Zhang, Z. Effect of Stress Triaxiality on Plastic Damage Evolution and Failure Mode for 316L Notched Specimen. *Metals* **2019**, *9*, 1067. [CrossRef]
12. Zhong, J.; Xu, T.; Guan, K.; Huang, L. Evaluation of Ductile Damage Parameters under High Stress Triaxiality. *Exp. Mech.* **2017**, *57*, 501–504. [CrossRef]
13. Yu, F.; Ben Jar, P.-Y.; Hendry, M. Constitutive analysis of pressure-insensitive metals under axisymmetric tensile loading: A stress triaxiality-dependent plasticity damage model. *Int. J. Mech. Sci.* **2018**, *142–143*, 21–32. [CrossRef]

14. Zhu, Y.; Engelhardt, M.; Pan, Z. Simulation of ductile fracture initiation in steels using a stress triaxiality–shear stress coupled model. *Acta Mech. Sin.* **2019**, *35*, 600–614. [CrossRef]
15. Coppola, T.; Cortese, L.; Folgarait, P. The effect of stress invariants on ductile fracture limit in steels. *Eng. Fract. Mech.* **2009**, *76*, 1288–1302. [CrossRef]
16. Thompson, R.D.; Hancock, J.W. Ductile failure by void nucleation, growth and coalescence. *Int. J. Fract.* **1984**, *26*, 99–112. [CrossRef]
17. Drucker, D.C.; Rice, R. Plastic deformation in brittle and ductile fracture. *Eng. Fract. Mech.* **1970**, *1*, 577–602. [CrossRef]
18. Pineau, A.; Benzerga, A.A.; Pardoen, T. Failure of metals I: Brittle and ductile fracture. *Acta Mater.* **2016**, *107*, 424–483. [CrossRef]
19. Cao, T.-S.; Gachet, J.-M.; Montmitonnet, P.; Bouchard, P.-O. A Lode-dependent enhanced Lemaitre model for ductile fracture prediction at low stress triaxiality. *Eng. Fract. Mech.* **2014**, *124–125*, 80–96. [CrossRef]
20. Kiran, R.; Khandelwal, K. A triaxiality and Lode parameter dependent ductile fracture criterion. *Eng. Fract. Mech.* **2014**, *128*, 121–138. [CrossRef]
21. Malcher, L.; Andrade Pires, F.M.; César de Sá, J.M.A. An extended GTN model for ductile fracture under high and low stress triaxiality. *Int. J. Plast.* **2014**, *54*, 193–228. [CrossRef]
22. Bao, Y.; Wierzbicki, T. On the cut-off value of negative triaxiality for fracture. *Eng. Fract. Mech.* **2005**, *72*, 1049–1069. [CrossRef]
23. Kubík, P.; Šebek, F.; Hůlka, J.; Petruška, J. Calibration of ductile fracture criteria at negative stress triaxiality. *Int. J. Mech. Sci.* **2016**, *108–109*, 90–103. [CrossRef]
24. Brünig, M.; Gerke, S.; Schmidt, M. Damage and failure at negative stress triaxialities: Experiments, modeling and numerical simulations. *Int. J. Plast.* **2018**, *102*, 70–82. [CrossRef]
25. Bonora, N.; Testa, G.; Ruggiero, A.; Iannitti, G.; Gentile, D. Continuum damage mechanics modelling incorporating stress triaxiality effect on ductile damage initiation. *Fatigue Fract. Eng. Mater. Struct.* **2020**, *43*, 1755–1768. [CrossRef]
26. Testa, G.; Bonora, N.; Ruggiero, A.; Iannitti, G.; Gentile, D. Stress triaxiality effect on void nucleation in ductile metals. *Fatigue Fract. Eng. Mater. Struct.* **2020**, *43*, 1473–1486. [CrossRef]
27. Testa, G.; Bonora, N.; Ruggiero, A.; Iannitti, G.; Gentile, D. Stress triaxiality effect on cleavage fracture stress. *Theor. Appl. Fract. Mech.* **2020**, *109*, 102689. [CrossRef]
28. Saeidi, N.; Ashrafizadeh, F.; Niroumand, B.; Forouzan, M.R.; Mohseni mofidi, S.; Barlat, F. Void coalescence and fracture behavior of notched and un-notched tensile tested specimens in fine grain dual phase steel. *Mater. Sci. Eng.* **2015**, *644*, 210–217. [CrossRef]
29. Khan, A.; Liu, H. A new approach for ductile fracture prediction on Al 2024-T351 alloy. *Int. J. Plast.* **2012**, *35*, 1–12. [CrossRef]
30. Driemeier, L.; Brünig, M.; Micheli, G.; Alves, M. Experiments on stress-triaxiality dependence of material behavior of aluminum alloys . *Mech. Mater.* **2010**, *42*, 207–217. [CrossRef]
31. Kim, H.; Kobayashi, T.; Niimoni, M.; Hagiwara, T.; Sakamoto, T. Effect of stress triaxiality on fracture behaviour of Al-Li system alloy . *Mater. Sci. Forum* **1996**, *217–222*, 1499–1504. [CrossRef]
32. Brünig, M.; Chyra, O.; Albrecht, D.; Driemeier, L.; Alves, M. A ductile damage criterion at various stress triaxialities. *Int. J. Plast.* **2008**, *24*, 1731–1755. [CrossRef]
33. Zhang, K.; Badreddine, H.; Hfaiedh, N.; Saanouni, K.; Liu, J. Enhanced CDM model accounting of stress triaxiality and Lode angle for ductile damage prediction in metal forming. *Int. J. Damage Mech.* **2021**, *30*, 260–282. [CrossRef]
34. Li, H.; Fu, M.; Lu, J.; Yang, H. Ductile fracture: Experiments and computations. *Int. J. Plast.* **2011**, *27*, 147–180. [CrossRef]
35. Yu, S.; Cai, L.; Yao, D.; Bao, Ch. Critical ductile fracture criterion based on first principal stress and stress triaxiality. *Theor. Appl. Fract. Mech.* **2020**, *109*, 102696. [CrossRef]
36. Bao, Y.; Wierzbicki, T. On fracture locus in the equivalent strain and stress triaxiality space. *Int. J. Mech. Sci.* **2004**, *46*, 81–98. [CrossRef]
37. Kou, L.; Zhao, W.; Tuo, X.; Wang, G.; Sun, C. Effect of stress triaxiality on fracture failure of 6061 aluminium alloy. *J. Mech. Eng. Sci.* **2020**, *14*, 6961–6970. [CrossRef]
38. Cao, T.-S.; Gaillac, A.; Montmitonnet, P.; Bouchard, P.-O. Identification methodology and comparison of phenomenological ductile damage models via hybrid numerical–experimental analysis of fracture experiments conducted on a zirconium alloy. *Int. J. Solids Struct.* **2013**, *50*, 3984–3999. [CrossRef]
39. Takuda, H.; Mori, K.; Hatta, N. The application of some criteria for ductile fracture to the prediction of the forming limit of sheet metals. *J. Mater. Process. Technol.* **1999**, *95*, 116–121. [CrossRef]
40. Canales, C.; Boman, R.; Ponthot, J.-P. Application of uncoupled damage models to predict ductile fracture in sheet metal blanking. *Key Eng. Mater.* **2016**, *725*, 483–488. [CrossRef]
41. Komori, K. Effect of ductile fracture criteria on chevron crack formation and evolution in drawing. *Int. J. Mech. Sci.* **2003**, *45*, 141–160. [CrossRef]
42. Yue, Z.; Cao, K.; Badreddine, H.; Saanouni, K.; Gao, J. Failure prediction on steel sheet under different loading paths based on fully coupled ductile damage model. *Int. J. Mech. Sci.* **2019**, *153–154*, 1–9. [CrossRef]
43. Gruben, G.; Hopperstad, O.; Børvik, T. Evaluation of uncoupled ductile fracture criteria for the dual-phase steel Docol 600DL. *Int. J. Mech. Sci.* **2012**, *62*, 133–146. [CrossRef]
44. Kiran, R.; Khandelwal, K. Experimental Studies and Models for Ductile Fracture in ASTM A992 Steels at High Triaxiality. *J. Struct. Eng.* **2014**, *140*, 04013044. [CrossRef]

45. Peng, Z.; Zhao, H.; Li, X. New ductile fracture model for fracture prediction ranging from negative to high stress triaxiality. *Int. J. Plast.* **2021**, *145*, 103057. [CrossRef]
46. Bonora, N. A nonlinear CDM model for ductile failure. *Eng. Fract. Mech.* **1997**, *58*, 11–28. [CrossRef]
47. McAllen, P.J.; Phelan, P. Ductile fracture by central bursts in drawn 2011 aluminium wire. *Int. J. Fract.* **2005**, *135*, 19–33. [CrossRef]
48. Celentano, D.; Chaboche, J. L. Experimental and numerical characterization of damage evolution in steels. *Int. J. Plast.* **2007**, *23*, 1739–1762. [CrossRef]
49. Freudenthal, A.M. *The Inelastic Behaviour of Engineering Materials and Structures*; John Wiley and Sons: New York, NY, USA, 1950.
50. Cockcroft, M.; Latham, D. Ductility and workability of metals. *J. Inst. Met.* **1968**, *96*, 33–39.
51. Chaouadi, R.; De Mester, P.; Vandermeulen, W. Damage work as ductile fracture criterion. *Int. J. Fract.* **1994**, *66*, 155–164. [CrossRef]
52. Ayada, M.; Higashino, T.; Mori, K. Central bursting in extrusion of inhomogeneous materials. *Adv. Technol. Plast.* **1987**, *1*, 553–558.
53. Gonzalez, A.; Celentano, D.; Cruchaga, M. Assessment of ductile failure models in single-pass wire drawing processes. *Int. J. Damage Mech.* **2017**, *27*, 1291–1306. [CrossRef]
54. Wang, T.-J. Unified CDM model and local criterion for ductile fracture—I. Unified CDM model for ductile fracture. *Eng. Fract. Mech.* **1992**, *42*, 177–183. [CrossRef]
55. Chandrakanth, S.; Pandey, P.C. An isotropic damage model for ductile material. *Eng. Fract. Mech.* **1995**, *50*, 457–465. [CrossRef]
56. La Rosa, G.; Mirone, G.; Risitano, A. Effect of stress triaxiality corrected plastic flow on ductile damage evolution in the framework of continuum damage mechanics. *Eng. Fract. Mech.* **2001**, *68*, 417–434. [CrossRef]
57. Chow, C.L.; Wang, J. An anisotropic theory of continuum damage mechanics for ductile fracture. *Eng. Fract. Mech.* **1987**, *27*, 547–558. [CrossRef]
58. Gonzalez, A.; Celentano, D.; Cruchaga, M. Bilinear damage evolution in AA2011 wire drawing processes. *Int. J. Damage Mech.* **2021**. [CrossRef]
59. *ASTM E8/E8M*; Standard Test Methods for Tension Testing of Metallic Materials. ASTM International: West Conshohocken, PA, USA, 2021.
60. Blaber, J.; Adair, B.; Antoniou, A. Ncorr: Open-Source 2D Digital Image Correlation Matlab Software. *Exp. Mech.* **2015**, *55*, 1105–1122. [CrossRef]
61. Huang, Y. Accurate dilatation rate for spherical voids in triaxial stress fields. *J. Appl. Mech.* **1991**, *58*, 1084–1086. [CrossRef]
62. Celentano, D. A large strain thermoviscoplastic formulation for the solidification of S.G. cast iron in a green sand mould. *Int. J. Plast.* **2001**, *17*, 1623–1658. [CrossRef]